Doctoral Dissertations and Master's Theses

Spring 5-2015

Modeling and Simulation of Radiation from Electronic Transitions in Hypersonic Atmospheric Reentry Flow

Curtis Scholz
Embry-Riddle Aeronautical University

Follow this and additional works at: https://commons.erau.edu/edt

Part of the Space Vehicles Commons

MODELING AND SIMULATION OF RADIATION FROM ELECTRONIC
TRANSITIONS IN HYPERSONIC ATMOSPHERIC REENTRY FLOW

A Thesis

Submitted to the Faculty

of

Embry-Riddle Aeronautical University

by

Curtis Scholz

In Partial Fulfillment of the

Requirements for the Degree

of

Master of Science in Aerospace Engineering

May 2015

Embry-Riddle Aeronautical University

Daytona Beach, Florida

MODELING AND SIMULATION OF RADIATION FROM ELECTRONIC TRANSITIONS IN HYPERSONIC ATMOSPHERIC REENTRY FLOW

by

Curtis Scholz

A Thesis prepared under the direction of the candidate's committee chairman, Dr. Eric Perrell, Department of Aerospace Engineering, and has been approved by the members of the thesis committee. It was submitted to the School of Graduate Studies and Research and was accepted in partial fulfillment of the requirements for the degree of Master of Science in Aerospace Engineering.

THESIS COMMITTEE

Member, Dr. Eric Perrell

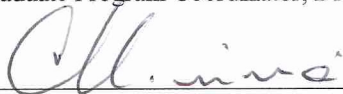Member, Dr. Lakshmanan Narayanaswami

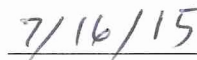Member, Dr. William Engblom

Department Chair, Dr. Anastasios Lyrintzis
or Graduate Program Coordinator, Dr.Yi Zhao
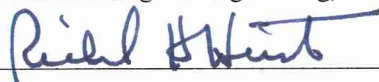
7/16/2015

Date

Dean of College of Engineering, Dr. Maj Mirmirani

7/16/15

Date

Associate VP for Academics, Dr. Robert Oxley

7/29/15

Date

ACKNOWLEDGMENTS

TABLE OF CONTENTS

LIST OF TABLES

LIST OF FIGURES

SYMBOLS

a_r	atomic radius, cm
A_{ul}	Einstein Coefficient for spontaneous emission, s^{-1}
B_{ul}	Einstein Coefficient for stimulated emission (frequency), $cm^2 erg^{-1} s^{-1}$
B_{lu}	Einstein Coefficient for absorption (frequency), $cm^2 erg^{-1} s^{-1}$
c_0	speed of light, 2.998×10^{10} cm/s
D	effective molecular collisional diameter, cm
e_l	lower energy level, cm^{-1}
e_u	upper energy level, cm^{-1}
g	molecular degeneracy, -
h	Planck's Constant, 6.626×10^{-27} erg s
I_{b_ν}	blackbody intensity, erg/cm^2
I_{b_λ}	blackbody intensity, erg/cm^3-s
I_{ν_0}	Incoming intensity, erg/cm^2-sr
k	Boltzmann's Constant, 1.3807×10^{-16} erg K^{-1}
m	molecular mass, g
n	molecules per unit volume, cm^{-3}
n	refractive index, -
n_a	number density of radiating species, cm^{-3}
p	probability function
P	atmospheric pressure, erg/cm^3
q_r	radiation heat flux, $(erg/s)/cm^2$
Re	Reynold's number, -
$\hat{s}$	unit vector into a given direction, -
S_ν	integrated line strength, 1/cm-s
T	temperature, K
U	free stream velocity vector, cm/s
v_e	electron velocity, cm/s
v_{em}	relative velocity of the emitter, cm/s
v_{em}	velocity of the emitter, cm/s
v_m	mean molecular velocity, cm/s
x	distance travelled through medium, cm
β_R	radiative thermal conductivity, $(erg/s)/cm$-K
γ	spectral line half-width, cm
γ_N	natural line half-width, s^{-1}
γ_C	collisional line half-width, s^{-1}
γ_L	Lorentzian line half-width, s^{-1}
γ_D	Doppler line half-width, s^{-1}
η	wavenumber, cm^{-1}
ε_λ	emission coefficient, erg/s-cm^3-μm-sr
ε_λ^c	assembled parameter emission coefficient, erg/s-sr
ε_λ^*	non-dimensionalized emission coefficient, erg/s-μm-sr

κ_R	Rosseland-mean absorption coefficient, cm^{-1}
κ_λ	absorption coefficient, cm^{-1}
κ_λ^c	assembled parameter absorption coefficient, cm^3
κ_λ^*	non-dimensionalized absorption coefficient, cm^2
λ	wavelength, cm
λ_0	centerline wavelength, cm
ν	Frequency, s^{-1}
σ	Stephen-Boltzmann's constant, 5.6704×10^{-5} erg/s-cm^2-K^4
ω	angular frequency, sr /s
ω_0	natural angular frequency, sr /s
Ω	solid angle, sr
$\phi_{L\lambda}$	normalized Lorentz line shape function, s
$\phi_{D\lambda}$	normalized Doppler line shape function, s
$\phi_{V\lambda}$	normalized Voigt line shape function, cm^{-1}

ABBREVIATIONS

CR	collisional-radiative model
DSMC	direct simulation Monte Carlo
LAURA	Langley Aero-thermodynamic Upwind Relaxation Algorithm
HARA	High Temperature Air Radiation Algorithm
MCM	Macroscopic Chemistry Method
ViSpeN	Vibrationally Specific Nitrogen
H	Hydrogen
N	Nitrogen
O	Oxygen
b-b	bound-bound transition
b-f	bound-free transition
f-b	free-bound transition
f-f	free-free transition
u-l	upper to lower energy level transition
l-u	lower to upper energy level transition

ABSTRACT

Scholz, Curtis MSAE, Embry-Riddle Aeronautical University, May 2015. Modeling and Simulation of Radiation from Electronic Transitions in Hypersonic Atmospheric Reentry Flow.

A capability for higher accuracy heat transfer modeling in CFD for hypersonic re-entry flows, via inclusion of thermal radiation, is sought. With temperatures reaching tens of thousands of degrees, radiation is known to be significant to chemical reaction rates and thermal boundary layer development, hence surface heat transfer and thermal ablation both to the heat shield and the backshell region of re-entry vehicles. Two current NASA solicitations seek such an improved capability relative to the Mars and Earth entry problems, as uncertainty typically leads to overdesign and excess weight. The present research develops a first physics-based "building block," which computes thermal radiation line strength distributions for certain species of interest. The spectral data required as inputs – electronic transition rates, energies, and wavelengths – for atomic nitrogen, oxygen, and hydrogen are obtained from a database maintained by NIST. Vibrational and rotational transitions of diatomic molecules are not addressed here. Absorption and emission coefficients are computed, hence an effective radiative thermal conductivity according to Rosseland is used in the "optically thick," or "diffusion" approximation. Absorption and emission coefficients compared respectably with other published results, discrepancies attributable to differing sources of input spectral data. The computational module was implemented in an in-house Navier-Stokes research code, and demonstrated on a 2D hypersonic flow over a blunt body. The radiative diffusion model reduced peak temperatures and thermal gradients, as expected.

1. Introduction

When analyzing hypersonic flow, such as that around a reentry vehicle entering the Earth's atmosphere, it is important to consider the effects of radiative heat transfer to be able to compute a more realistic temperature field. This is because as higher temperature fields develop around aerospace reentry vehicles, radiation becomes a more significant contribution to the total heat transfer observed by the structure, as is easily surmised from the Stephen-Boltzmann law:

$$q_r = \epsilon \sigma T^4 \tag{1.1}$$

As the flow Mach number increases radiation comprises a greater percentage of the net heat transfer observed by a reentry vehicle, by as much as an order of magnitude (Anderson, 2006).

The physics of radiation heat transfer is complex. One might categorize physical considerations under the following headings:

1. surface geometries and properties

2. transitions between energy levels (electronic, vibrational, rotational) in participating media

3. equilibrium or non-equilibrium of same

4. propagation of radiative energy (or fluxes).

We wish to build a set of computational tools for simulating flows with radiative heat transfer, using a modular, or "building block" approach, eventually to treat all of these considerations via modeling as close to physical first principles as practicable. Two current NASA research solicitations seek to develop such computational capabilities beyond those of the, "legacy codes."

We follow the approach of much earlier efforts which produced a computational tool for another conjugate heat transfer mechanism, solid conduction (Fletcher, 2007; Engblom, Fletcher, Georgiadis, 2007). For these studies an in-house research CFD code was used as a development platform, and the resulting "compute engine" subsequently interfaced with the Wind-US CFD code (Perrell, Power, Robinson, 2010).

Previous work under the first heading successfully addressed surface-to-surface radiative transfer with non-participating media using a discretized view factor network for black- or gray-body surface mesh cells. (Nutzati Fontaine, 2013; Nutzati Fontaine and Perrell, 2013).

The present study explores radiative transfer in participating media (heading 2), modeling electronic transitions in atomic species. A database of atomic transition line-center frequencies will be constructed for species of interest. Line-broadening will be modeled, in order that continuous frequency spectra might be considered in subsequent studies. Molecular transitions are also deferred to subsequent studies, as are non-equilibrium energy levels (heading 3). A popular, albeit simplistic treatment of the radiative fluxes (heading 4) is used (Rosseland, 1936). Here radiation is assumed to propagate diffusely, as opposed to directionally, via ray-tracing or Monte-Carlo methods.

We attempt also to present the governing equations with *substantive* explanations. We find these to be lacking in the engineering literature. In particular, cavalier switching of spectral variables, uncertain use of distributed versus line-center values, uncertain angular dependencies, notations with duplicate definitions, apparent dimensional inconsistencies, and poor motivation from a physicality perspective, are pervasive.

Finally, the computational module will be demonstrated on a simple blunt body in

hypersonic flow. It has been observed of hypersonic reentry vehicles that the more

"blunt" the body in the flow, the more air that would be trapped in front of the vehicle.

This leads to effectively creating a bubble on the nose of the blunt-body which pushes

back the heated shockwave from the aerospace structure. As shown by Allen and Eggers

(1953), the aerodynamic drag coefficient is inversely proportional to the heat load, thus

the detached shockwave seen on the blunt body configuration experiences less heating

than the traditional shapes.

2. Background

Other models have been used to analyze vibrational modes of excitation for radiation. The collisional-radiative (CR) model is a commonly used model for this purpose and has been implemented to simulate re-entry on Saturn's moon Titan (Brandis, Laux, Magin & McIntyre, 2014). The input data for molecular excitation rates and characteristics was attained from the Non-Equilibrium Air Radiation (NEQAIR) code (Whiting, Park, Liu, Arnold, & Paterson, 1996). NEQAIR is a tool developed by NASA that requires a user input of the thermodynamic properties of air under specific conditions to determine radiative properties. As CR models are generally used for modeling non-equilibrium, it is a useful tool when considering an atmosphere which contains non-equilibrium molecular populations (CN and N_2 for Titan). Since this research focuses on diatomic molecules, vibrational transitions are the dominant model of radiation and thus a vibrational excitation model is required. The CR model utilizes a system of rate equations which consider all of the possible reactions between the internal energy levels of atoms and molecules. This is used to compute a wider range of reactions, and is not limited by the Boltzmann distribution assumption (assumes a fixed composition and thermal equilibrium). This is used alongside the Vibrationally Specific Nitrogen (ViSpeN) (Pierrot, Laux,, & Kruger, 1998) CR model to analyze the atmospheric entry conditions. However, it is later mentioned "large variations exist in predictions for radiation levels from CFD…" (Brandis, Laux, Magin & McIntyre, 2014).

Research has also been done on analyzing radiation induced from shock-tubes using the Macroscopic Chemistry Method (MCM) (Goldsworthy, 2012). MCM is an improvement on traditional DSMC to allow for chemistry modeling (DSMC-MCM). This

research utilized Boltzmann velocity distributions for particle collisions to model radiation. Although this research modelled radiation using DSMC-MCM (high computational time and power required), it was still found that the radiation model used "…the macroscopic models given here, would most likely begin to break down" (Goldsworthy 2012).

Three-dimensional ray tracing methodologies have also been used to model radiative heating in hypersonic shock layers (Mazaheri, Johnston, & Sefidbakht, 2013). In this research, Langley Aero-thermodynamic Upwind Relaxation Algorithm (LAURA) (Mazaheri, 2010) and High Temperature Air Radiation Algorithm (HARA) (Johnston, 2006) are used (both assume tangent slab radiative flux) to model radiation in Earth and Mars re-entry flows. Additionally, a case considering an optically thick medium was used for modelling the Mars-Earth entry simulation. However, to more accurately calculate the radiative heating, HARA is coupled with ray tracing techniques. This is done to eliminate the error generally assumed with codes that use the tangent slab radiative flux, and create a more efficient model. Ray tracing models the paths of individual particles or electromagnetic waves to compute absorption and emission coefficients.

Sohn has successfully clarified the modeling process for electron transitions (Sohn, 2011) (Li, Ozawa, Sohn, & Levin, 2011). While Sohn uses more computationally intensive models for simulation that this research considers (DSMC and CR), the research he is involved with provides useful comparison and discussion of electronically excited modeling practices. Sohn's results provide reliable absorption and emission data which he validates against NEQAIR with high fidelity. It is because of this that this research follows the more general modelling practices and techniques laid out by Sohn.

While a few published examples of radiation modeling exist, a large majority of publications utilize the radiation tool NEQAIR. The publications that have developed a CFD code have utilized either Monte Carlo variants (most generally DSMC) or ray-tracing models. However, though this high level modeling undoubtedly has the capability of yielding higher fidelity results, the majority of these authors have failed in demonstrating a coherent process of modeling radiation for electronic transitions. Furthermore, each of these methods is highly computationally intensive. By developing line-by-line radiation modules for the CFD code used in this research, the framework for more complex radiation has been constructed.

3. Physics of the Problem

Thermal radiation results from changes in atomic and molecular energy levels. These changes consist of both spontaneous and induced transitions of the electrons which exist in these energy levels. The energy levels of atoms and molecules are quantized. That is, they are capable of existing only in a finite set of energy values. These energy levels are unique to each molecular species, dependent on their atomic and molecular structure. Of these energy levels, the lowest of level is referred to as the ground state for the atom. All energy levels that exist above this ground state are referred to as excited states.

The energy of an atom or molecule is defined in reference to the ground state, which is composed of four different energy contribution sources; electronic, vibrational, rotational, and translational. This research focuses on monatomic species common to reentry in Earth's upper atmosphere (N, O, and H). Monatomic species have no rotational or vibrational energy since there exists no molecular bond for the secondary atom to vibrate or rotate about. Thus, when considering monatomic molecules, the only relevant form of energy level excitation comes from the electronic excitations.

The electron energy levels are given by the arrangement of electrons in a number of different shells and sub-shells for a particular atom. The closer the shell is to the nucleus of the atom, the lower the energy of the electron (lower energy level). As the shells and subshells move outward from the center of the atom, the energies of the electrons that populate them increase. If an electron absorbs or emits radiation of the correct thermal photon energy, it moves to a different shell or sub-shell in the atom. This change in orbital radius of an electron is referred to as an electron transition. The energy

of an emitted or absorbed photon is simply the difference between the upper and lower

energy levels.

$$e_u - e_l = hv \tag{3.1}$$

where h is Planck's constant and v is the frequency of the electromagnetic wave.

There are three processes by which electron transitions occur: spontaneous emission,

stimulated emission (sometimes referred to as negative absorption), and absorption. Each

of these three modes of transition is the result of a specific electron event. The first of

these is a bound-bound (b-b) transition, which considers transitions between two atomic

or molecular energy levels. A non-dissociated atomic energy level is commonly referred

to as a *bound* level. Conversely, electrons can also exist in a dissociated atomic level,

referred to as a *free* level, due to ionization. The next transition has two forms, a bound-

free (b-f) transition which considers a transition from a bound level to a free level

(absorption) and free-bound (f-b), which works inversely (emission). Finally, transitions

between two free atomic levels are called free-free (f-f) transitions. This model considers

purely atomic species, for which, bound-bound transitions produce the most dominant

contribution to the overall thermal radiation (Sohn, 2011). It is for this reason that bound-

free and free-free transitions were not considered, and the radiation was calculated purely

from bound-bound transitions.

Now, consider a molecule having some known upper and lower energy levels u

and l. The number of transitions that occur from a particular level u to level l due to the

release of a photon, with energy packet hv (a spontaneous emission), is directly

proportional to the number of atoms or molecules at that energy level. The spontaneous

emission event is isotropic, such that the direction of the emitted photon is random

yielding equal emission intensity in all directions. This emission event is shown below in Figure 3.1(a). In addition to spontaneous emission events, it is postulated from quantum mechanics that if some radiative intensity, or photon stream, with the appropriate frequency interacts with an atom, it will emit photons in the same direction as the incoming radiative intensity. This event is classified as a stimulated emission, which combined with the spontaneous emission event yields the total emission for a particular line transition. This stimulated emission event is illustrated below in Figure 3.1(b).
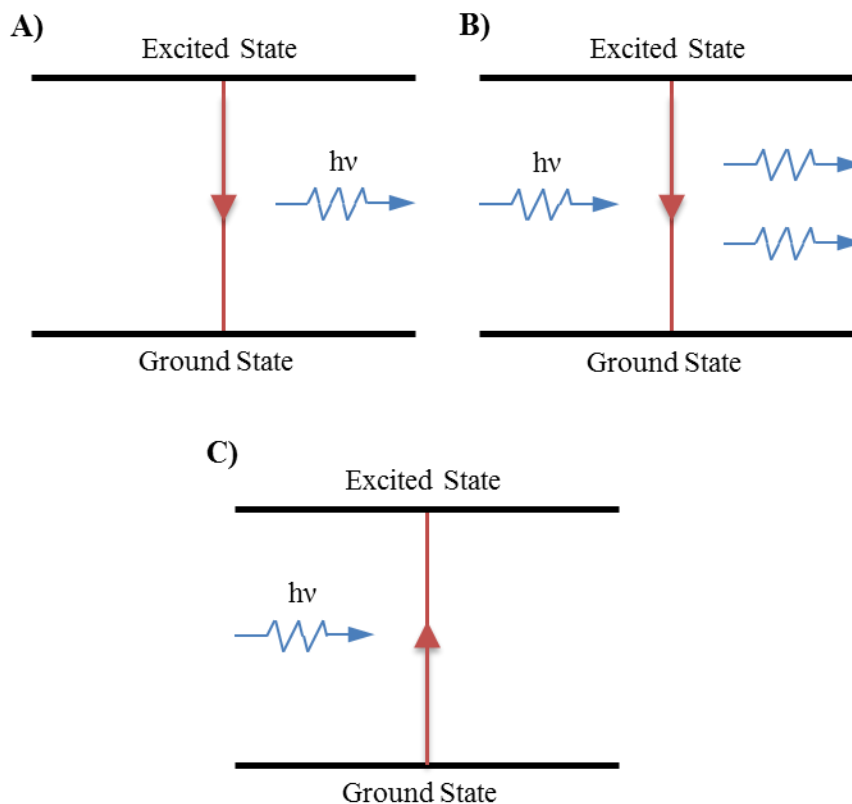
Figure 3.1 (a) spontaneous emission, (b) stimulated emission, and (c) absorption events

The final electronic excitation relationship to be considered is absorption, or the capture of a photon traveling at the appropriate frequency. The rate of absorption in a

particular medium is proportional to the strength of the incoming radiation as well as the number of electrons in the lower energy level *l*. An illustration of this absorption event is shown above in Figure 3.1(c). The Einstein probabilities for each of these electron transition modes are defined around a single particular transition frequency, or natural frequency. However, the probability of these events is distributed over a frequency range. This is due to broadening around the natural frequency line center.

Thermal radiation energy can be characterized by two different terminologies depending on the theory used to describe them. These two theories are electromagnetic wave theory and quantum mechanics. The first theory models the thermal radiation energy as electromagnetic waves, while the second considers the radiation energy as consisting of massless energy parcels, or photons. However, neither of these completely describes the phenomenon that is radiation heat transfer, thus these terms will be used interchangeably. Electromagnetic waves, or photons, travel through any medium at the speed of light, since it exists in the electromagnetic spectrum. The speed of light is dependent on the medium it travels through, and is related to the speed of light in a vacuum through the following;

$$c = \frac{c_0}{n}$$
(3.2)

Where *n* is the refractive index, and is treated as unity for a vacuum. For this study, an upper atmospheric reentry will have a near unity refractive index due to the thin atmosphere. Thus, for simplicity, the speed traveled by the photons will be considered to be the vacuum speed of light 2.998 x 10^{10} cm/s.

Energy contained in a photon is directly proportional to the frequency, as seen in Equation (3.1). Electromagnetic waves can be characterized using any of the four

spectral variables to perform line broadening across: wavelength (λ), wavenumber (η), frequency (ν), or angular frequency (ω). All of these spectral variables can be simply converted to the others through the following relationships;

$$v = \frac{\omega}{2\pi} = \frac{c}{\lambda} = c\eta \tag{3.3}$$

The comparison of the orders of magnitude among these variables is shown below in Figure 3.1.
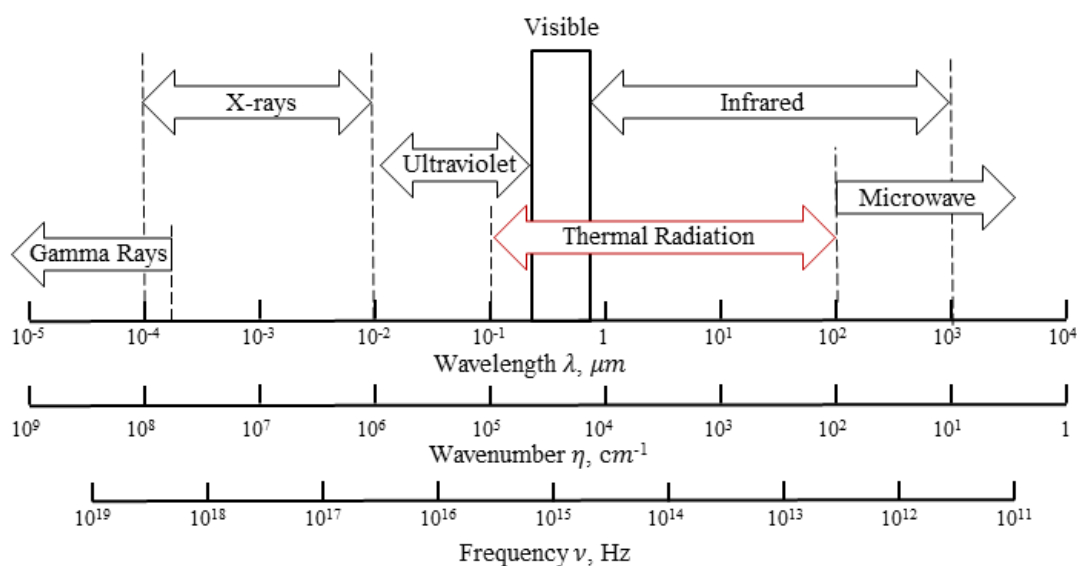
Figure 3.2 Scales of spectral variable scales over the radiation spectrum

Transition rates for emissions and absorption are properties which depend on the atom and the frequency. These are called, "Einstein Coefficients". National Institutes of Standard (NIST) maintains databases of these [www.NIST.gov]. In reality though, frequency of radiation from a particular electronic transition is not a discrete value, but is distributed about the "line center" frequency. This distribution is called, "line broadening", mechanisms for which include Doppler Effect, molecular collision, and natural broadening associated with the Heisenberg's uncertainty principle. Use of these

concepts in computing radiative thermal transport is developed in the following section.

The transitional probability curve is developed from *line broadening* methodologies, and is accounted for through several different modeling techniques. Through the use of line broadening, the emission and absorption coefficients for a particular line transition can be determined. Once these absorption and emission coefficients have been independently computed, they are able to be combined into a single absorption coefficient via the diffusion approximation.

The diffusion approximation considers a specific region of the hypersonic flow to better simplify the media. While radiation's contribution in supersonic flow is considered to be more or less negligible (dominated by molecular viscous transport), it becomes the dominant mode of heat transfer in hypersonic flow. When this happens, the gases surrounding the reentry vehicle can be split into two regions, optically thin and optically thick. In optically thin media, the gas does not reabsorb, and just emits the radiation. In an optically thick media, the fluid element considered absorbs an amount of radiation and subsequently re-radiates the energy equally in all directions.

The diffusion approximation weights each of the individual absorption coefficients via the black-body intensity and combines them to formulate a single absorption coefficient for the molecular species. This absorption coefficient is called the Rosseland-mean absorption coefficient, and is used to determine the radiative thermal conductivity.

4. Governing Equations

4.1. Electronic Transitions

Radiation occurs due to transitions of electrons between energy levels. The first type of transition to be discussed is spontaneous emission, which is the random decay of electrons in excited energy levels to lower energy levels.

$$\left(\frac{dn_u}{dt}\right)_{u\to l} = -A_{ul}n_u \tag{4.1}$$

Here, A_{ul} is the proportionality constant known as the Einstein coefficient for spontaneous emission which has units of per second and n_u is the number density of atoms at the upper level U. The second mode of transitioning an electron from an upper to a lower energy level is via a stimulated emission event:

$$\left(\frac{dn_u}{dt}\right)_{u\to l} = -n_u B_{ul} \int_{4\pi} I_{v_0}\, d\Omega \tag{4.2}$$

where B_{ul} is the Einstein coefficient for stimulated emission, which has units that depend on the spectral variable, and I_{v_0} is the incoming intensity which is integrated over all Ω directions. During each u-l transition (for both stimulated and spontaneous emission), a photon is generated from the upper energy level. The energy released per unit time and volume is $n_u A_{ul} hv$.

Lastly, the rate of change of electrons from a lower to an upper energy level (an absorption event) is seen defined below in Equation (4.3).

$$\left(\frac{dn_u}{dt}\right)_{l\to u} = n_l B_{lu} \int_{4\pi} I_{v_0}\, d\Omega \tag{4.3}$$

Here, the proportionality coefficient B_{lu} is the Einstein coefficient for absorption. It can be shown from Planck's law the Einstein coefficients are related through the

following two equations:

$$A_{ul} = \frac{8\pi h c_0}{\lambda^3} B_{ul} \tag{4.4}$$

$$g_u B_{ul} = g_l B_{lu} \tag{4.5}$$

Here, g_u and g_l are the molecular degeneracies of the upper and lower energy levels, respectively. The molecular degeneracy is the number of ways electrons are able to exist at a discrete energy level. Now, considering solely the induced electron transitions (absorption and stimulated emission), the rate of change of the population density can be written as:

$$\frac{dn_u}{dt} = (n_l B_{lu} - n_u B_{ul}) \int_{4\pi} I_{\nu_0} \, d\Omega \tag{4.6}$$

By restricting the intensity to a single direction, this can be reduce to:

$$\frac{d}{d\Omega} \frac{dn_u}{dt} = (n_l B_{lu} - n_u B_{ul}) I_{\nu_0} \tag{4.7}$$

The LHS of the above equation is the rate of l-u transitions per volume in a particular direction, carrying units of s^{-1} cm^{-3} sr^{-1}. Now, considering that each l-u transition removes a photon $h\nu$:

$$h\nu \frac{d}{d\Omega} \frac{dn_u}{dt} = h\nu \, (n_l B_{lu} - n_u B_{ul}) I_{\nu_0} \tag{4.8}$$

This relationship now carries units of erg cm^{-3} s^{-1} sr^{-1}, which is simply the rate of absorption of incident intensity at frequency ν per unit depth in the Ω direction $I(\nu, \Omega)$. This value is equal and opposite to the rate of attenuation of $I(\nu, \Omega)$ in its direction of propagation:

$$\frac{dI(v,\Omega)}{dx} = -hv\,(n_l B_{lu} - n_u B_{ul})I_{v_0} \tag{4.9}$$

It is crucial to carefully distinguish the difference between $I(v,\Omega)$ and I_v. $I(v,\Omega)$ is a function of the incident angle of the incoming intensity a frequency v whereas I_v is the differentiation incoming intensity with respect to the spectral variable (v). Now, calling the terms that pre-multiply the spectral intensity the integrated line strength (S_v), carrying units of cm^{-1} s^{-1}, or

$$S_v = (g_l n_l B_{lu} - g_u n_u B_{ul})hv \tag{4.10}$$

Equation (4.9) can be rewritten as

$$\frac{dI(v,\Omega)}{dx} = -SI_{v_0} \tag{4.11}$$

This shows that the integrated line strength is a rate coefficient that, when multiplied by the spectral intensity I_v, gives the rate of attenuation of intensity I at frequency v. By differentiating both sides with respect to v, the following relationship is developed:

$$\frac{d}{dv}\frac{dI}{dx} = -\frac{dS_v}{dv}I_v \tag{4.12}$$

$$\frac{dI_v}{dx} = -\kappa_v I_v \tag{4.13}$$

Equation (4.13) is the Beer-Lambert law, with κ_v being the absorption rate coefficient for spectral intensity I_v and having units of cm^{-1}. It is important here to note the relationship between the absorption rate coefficient and the integrated line strength as shown in these two equivalent expressions:

$$\kappa_v = \frac{dS_v}{dv} \tag{4.14}$$

$$\kappa_v = S_v \phi_v \tag{4.15}$$

It is important to distinguish that the subscripts used in the above equations indicate functionality with respect to frequency and *not* differentiation. In Equation (4.15), the variable ϕ_v has been introduced, which is the probability distribution function for intensity about a specific line center, such that the integration over the entire spectrum is unity.

$$\int_{\Delta v} \phi_v dv = 1 \tag{4.16}$$

These probability distribution functions are defined differently depending on the source of the line broadening. Different line broadening methodologies will be discussed further in the next section.

It should be noted that both stimulated emission and absorption events are dependent on the total incoming spectral intensity into the medium (I_{v_0}). This intensity is not a function of the media, but rather solely dependent on the frequency at which it is observed. However, the *absorbed* intensity (I_v) which passes through a given medium considers both the absorption coefficient as well as the distance traveled (x) through the media in addition to the incoming intensity. This resultant absorbed intensity is computed using Beer's law, defined in Equation (4.17). A visualization of Beer's law and how it is applied is shown below in Figure 4.1.

$$I_v = I_{v_0} e^{-\kappa_v x} \tag{4.17}$$
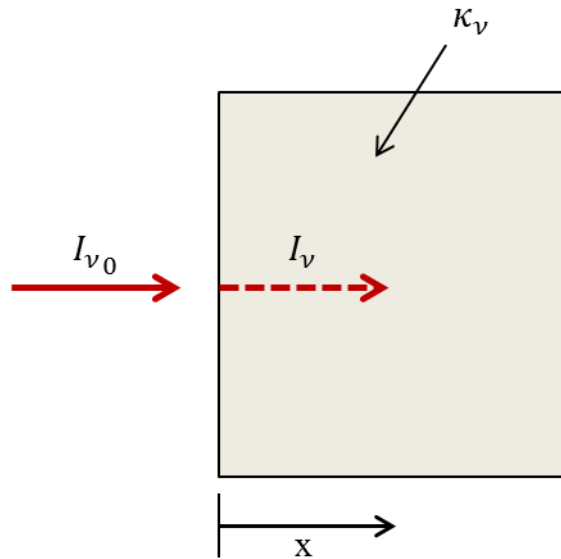
Figure 4.1 Illustration of Beer's Law

4.2. Spectral Line Broadening

The next step in this modeling sequence is to begin utilizing broadening

distributions to determine the transitional probabilities. The general variant of the

broadening functions begins with the normalized line shape function (ϕ_L) or profile. This

normalized profile is a probability distribution for the different transitions, and is defined

in the following Lorentz profile with respect to the frequency (Park, 1990);

$$\kappa_{Lv} = S_v \phi_L(\gamma, \Delta v)$$
(4.18)

$$\Delta v = v - v_0$$
(4.19)

where γ is the line half-width, v is the frequency, v_0 is the natural frequency for a

particular molecule, and S is the integrated line strength. Upon substitution of the

Lorentzian line shape function, the Lorentzian profile can be rewritten as:

$$\kappa_{L\nu} = \frac{S_\nu}{\pi} \frac{\gamma_L}{(\Delta\nu)^2 + \gamma_L{}^2} \qquad (4.20)$$

Finally, the line strength, defined in Equation (4.14), can be written as the integration of a single line absorption coefficient over the entire frequency spectrum, as shown below in Equation (4.21).

$$S \equiv \int_{\Delta\nu} \kappa_{L\nu} d\nu \qquad (4.21)$$

For this study, it was of interest to consider wavelength as the dependent spectral variable, thus a conversion of the above equations from frequency is required. Recalling from Equation (3.3), frequency and wavelength are inversely related to each other ($\nu = c_0/\lambda$). It should be noted that in doing this, the units of the normalized line profile remain seconds (units of inverse spectral variable, in this case frequency). This was done to ensure unit compatibility between the broadening term ($\Delta\nu$) and the line half-width.

Since the line half-width is classically defined (for frequency) to represent units of s^{-1}, in order to change the dependent spectral variable for the line profile, one must also convert the line half-width. The complication in doing this however, is due to it being defined independently of the spectral variable. This forces the development of "conversion factors" that need to be multiplied through the line half-widths for compatibility. While some sources have performed conversions on the line half-width to make these conversions, these are not well documented for wavelength (which complicates the relationship due to its inverse proportionality to frequency). In order to ultimately return to proper units while considering wavelength, a conversion is made on the final step of determining the line absorption coefficient. This result was validated

against methodology which considered the aforementioned conversions and yielded identical values.

In order to be able to create a complete and accurate line intensity profile for a given molecule across a spectral variable, multiple forms of line broadening techniques are considered. It was decided to consider the highest-contributing line broadening mechanisms to identify the spectral intensity profile; natural line broadening, collisional (pressure) line broadening, and Doppler broadening. The line shape profiles for collisional and natural broadening are Lorentzian as defined above. Doppler broadening utilizes a Gaussian distribution.

Natural line broadening is a manifestation of Heisenberg's uncertainty principle. The line half-width γ_N for this broadening method is the Einstein coefficient A_{ul}. The line half-width (γ_C) for this broadening profile is calculated from kinetic theory as (Penner, 1959):

$$\gamma_C = \frac{2}{\sqrt{\pi}} \frac{D^2 P}{\sqrt{mkT}} \qquad (4.22)$$

where D is the effective collisional diameter of a molecule, P is the pressure, c_0 is the speed of light in a vacuum, m is the molecular mass of the molecule in grams, k is the Boltzmann's constant and T is temperature in Kelvin. The convolution of two Lorentzian profiles is also a Lorentzian profile with half-width equal to the sum of the individual half widths.

$$\gamma_L = \gamma_N + \gamma_C \qquad (4.23)$$

However, the average time for a spontaneous emittance (natural broadening) to occur is much larger than the average time lapse between molecular collisions ($t_N \gg t_C$).

This large time lapse difference in emission events results in the half-width natural line broadening being invariably small in comparison to that for collisional broadening. For this reason, γ_N is omitted ($\gamma_L \cong \gamma_C$).

The spectral data for N, O, and H were acquired from NIST and databased respectively for the strong lines of neutral atoms (Sansonetti, J., & Martin, W.). In addition to spectral data, it was necessary to acquire effective diameters for each of the atoms being considered. For simplicity, the atoms were considered to be "hard spheres", meaning that the effective diameter would be defined as:

$$D = 2r_a \tag{4.24}$$

The atomic radii necessary for computing the effective diameters were supplied from empirical data published in the Journal of Chemical Physics (Slater 1964). A sample data set for atomic Oxygen that was used in this research can be seen below in Table 4.1.

Table 4.1 Data set example for strong lines of atomic Oxygen

Wavelength (λ) (cm)	Einstein Coeff (Aki) (10^8 s^{-1})	Degeneracies	Energy Levels (cm^{-1})	Atomic Configuration
1.30217E-05	3.15	5	0	2s22p4
		3	76794.978	2s22p3(4S−)3s
1.30486E-05	1.87	3	158.265	2s22p4
		3	76794.978	2s22p3(4S−)3s
1.30603E-05	0.623	1	226.977	2s22p4
		3	76794.978	2s22p3(4S−)3s
7.77194E-05	0.369	5	73768.2	2s22p3(4S−)3s
		7	86631.454	2s22p3(4S−)3p
0.000131649	0.119	9	88631.146	2s22p3(4S−)3p
		3	96225.049	2s22p3(4S−)4s

To illustrate and verify the line broadening model, the atomic lines for Nitrogen were broadened using the Lorentzian profile, considering both collisional and natural broadening effects. These line-shape profiles (ϕ_ω) were constructed for each of the three atomic species of interest (N, O, and H). That for Nitrogen is illustrated below in Figure 4.2. To better observe line broadening effects, a logarithmic scale was used.
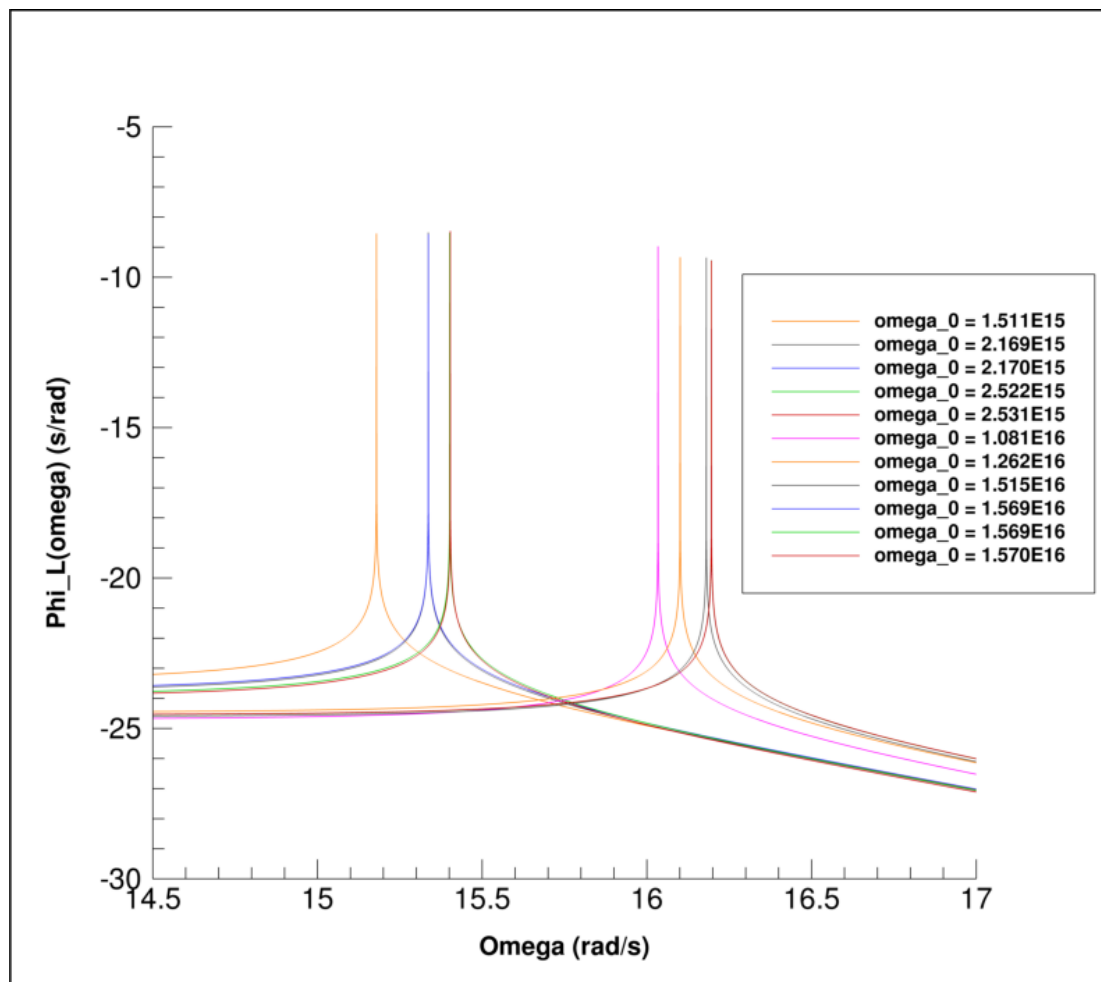
Figure 4.2 Lorentzian line shape broadening (ϕ_ω) for strong line of atomic Nitrogen

The individual Lorentzian profiles are weighted by their line strengths and added to create a single profile for the probability distribution (κ_ω), as seen below in Figure 4.3.
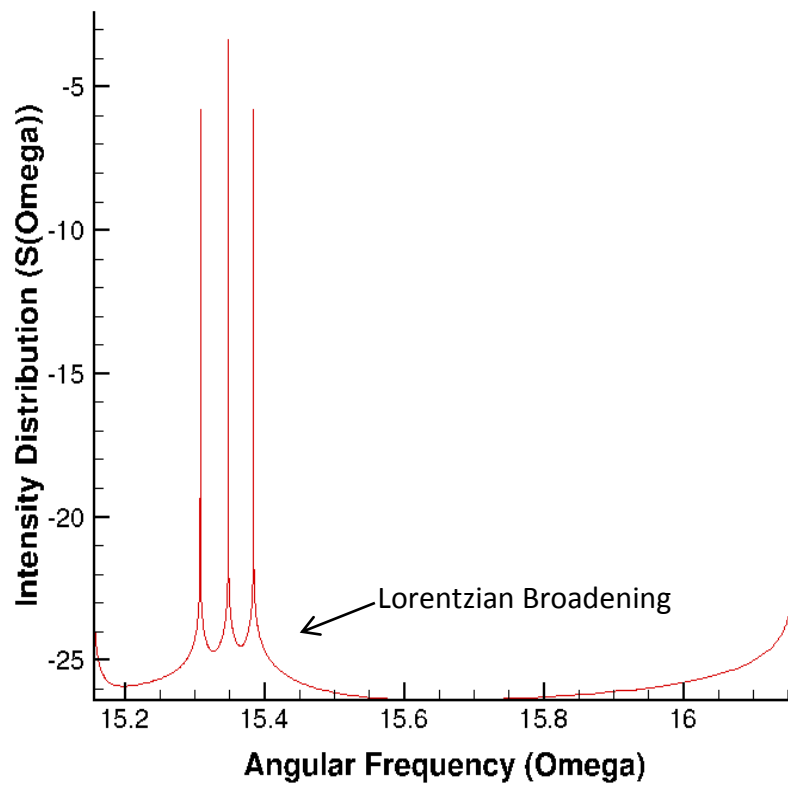
Figure 4.3 Logarithmic plot of Lorentzian intensity profile for atomic Nitrogen

A third model for line broadening is Doppler broadening, which utilizes a different model to define its line shape profile. For this broadening, the discrepancy between the observed and emitted wavelength is considered, and is dependent on the relative velocity as follows (Modest, 2013):

$$\eta_{obs} = \eta_{em}\left(1 + \frac{v_{em} \cdot \hat{s}}{c}\right) \tag{4.25}$$

Rewriting with respect to frequency yields:

$$\nu_{obs} = \nu_{em}\left(1 + \frac{v_{em} \cdot \hat{s}}{c}\right) \tag{4.26}$$

Where v_{em} is the velocity of the emitter, $\hat{s}$ is the unit vector that points from the

emitter to the observer, and c is the speed of light (as previously mentioned, for our case

this should be treated to be simply vacuum speed of light, c_0). Now, assuming a local

thermodynamic equilibrium, the Maxwell's velocity distribution may be used to

determine the probability for a relative velocity, $\hat{v}_{em} = v_{em} \cdot \hat{s}$ that exists between an

emitting/absorbing molecule and the observer. This probability distribution applied to the

velocity of a molecule in an ideal gas is defined as:

$$p(\hat{v}_{em}) = \left(\frac{m}{2\pi kT}\right)^{1/2} \exp\left(-\frac{m\hat{v}_{em}^2}{2kT}\right) \tag{4.27}$$

Using this velocity probability function $p(\hat{v}_{em})$ at small $\hat{v}_{em}$, the Doppler shift in

frequency is $\Delta v = v_0 \frac{\hat{v}_{em}}{c_0}$. Substitution of this shift into Equation (4.27) yields the

Doppler broadening line profile (Penner, 1959).

$$\kappa_{Dv} = S\phi_{Dv}(\gamma_D, \Delta v) = S\frac{\sqrt{\ln 2}}{\gamma_D\sqrt{\pi}}\exp\left[-\ln(2)\left(\frac{\Delta v}{\gamma_D}\right)^2\right] \tag{4.28}$$

The Doppler line half-width γ_D has units of s^{-1} (same as collisional and natural

line half-widths). This line half-width is a function of the frequency as well as the mean

molecular velocity (v_m):

$$\gamma_D = \frac{v_0}{c_0}v_m\sqrt{\ln(2)} \tag{4.29}$$

Or as defined by Modest:

$$\gamma_D = \frac{v_0}{c_0}\sqrt{\frac{2kT}{m}\ln(2)} \tag{4.30}$$

Here, v_0 is the natural frequency for the particular line transition, k is the

Boltzmann's constant, T is the temperature in Kelvin, and m is the mass of the molecule.

As before, the Doppler line half-width is put in terms of wavelength:

$$\gamma_D = \frac{1}{\lambda_0} \sqrt{\frac{2kT}{m} \ln(2)} \tag{4.31}$$

Now that both of the critical line broadening techniques (Lorentzian and Doppler) have been defined, it is necessary to combine these models so that a single model can be used in the radiative calculations. First, a comparison is shown between these two broadening techniques, demonstrating their behaviors over the temperature range as seen below in Figure 4.4. Due to the flow field dependency of the Lorentzian profile from collision broadening, γ_C will change proportionally such that a decrease in pressure will result in a decrement of γ_C and vice versa.
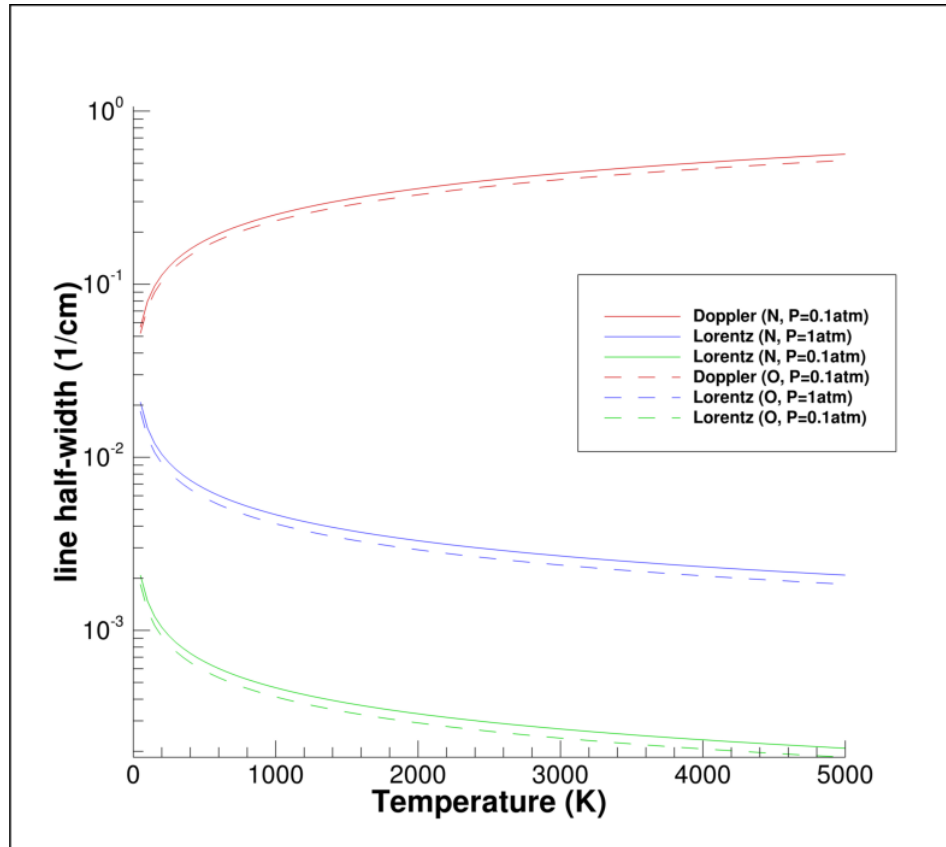
Figure 4.4 Comparison of Lorentzian line half-width and Doppler line half-widths

For most general engineering applications the Lorentzian half-width functions as the most important broadening mechanism to describe the line shape. However, at very high temperatures, the effect of the Doppler line half-width becomes comparable and event dominant. The profile which considers both the Lorentzian and Doppler line broadening profiles is called the Voigt profile, and is defined as (Goody & Yung, 1995);

$$\kappa_\nu = S_\nu \phi_{V_\nu}(\Delta\nu, \gamma_L, \gamma_D) = \frac{S_\nu \gamma_L}{\gamma_D^2 \pi^{\frac{3}{2}}} \int_{-\infty}^{+\infty} \frac{e^{-x^2}}{\left(\frac{\Delta\nu}{\gamma_D} - \frac{x}{\sqrt{\ln(2)}}\right)^2 + \left(\frac{\gamma_L}{\gamma_D}\right)^2} dx \qquad (4.32)$$

$$x = \frac{\hat{v}_e}{\sqrt{\dfrac{2kT}{m}}} = \frac{\hat{v}_e}{v_m} \tag{4.33}$$

The above equation considers two distribution functions: the first as a function of the spectral variable (coefficients leading the integral), and the second a function of the proportional electron-molecule velocities (integral). The Voigt profile is characterized by the fractional relationship between the Lorentzian line half-width and the Doppler line half-width (γ_L/γ_D), shown in Figure 4.5. This figure illustrates the characteristics of the Voigt profile as the region between a Doppler broadening dominant upper limit down to a Lorentzian broadening dominated lower limit.
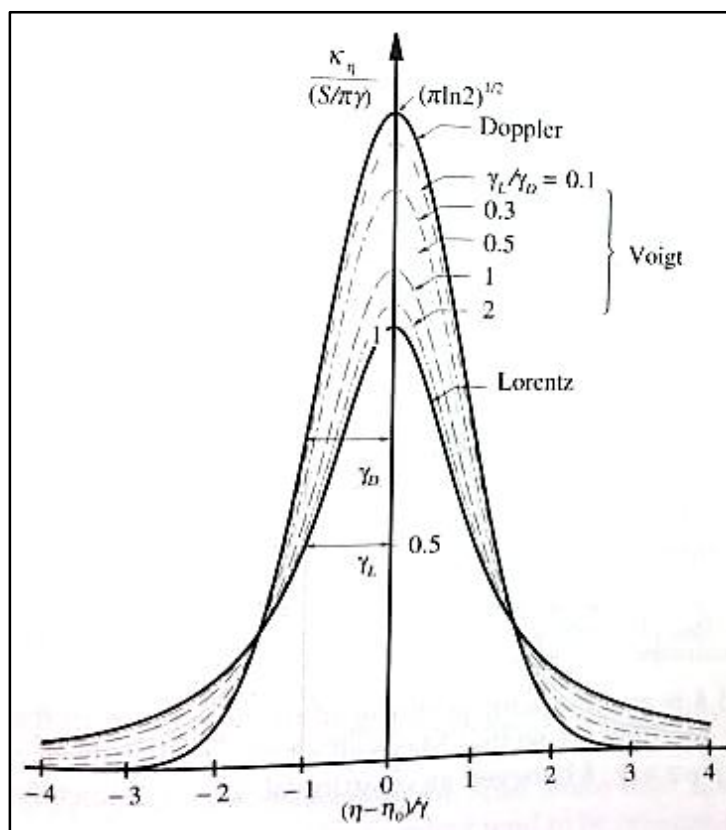
Figure 4.5 Comparison of Lorentzian, Doppler, and Voigt intensity profiles (Modest, 2013)

However, due to modeling limitations, the broadening aspect of this analysis was limited to being simply based around the natural wavelengths (λ_0). Because of this, rather than integrating over the entire spectrum of wavelengths, a discrete summation was performed of the natural wavelengths. This "normalizes" the Voigt profile such that the integral goes to unity, and the resultant profile is simplified to being purely a function of the Lorentzian and Doppler line half-widths. This reduces the above equation to the following form (Huang and Yung, 2003):

$$\kappa_{v_v} = S_v \phi_{V_v}(\gamma_D, \gamma_L) = \frac{S_v}{\pi^{3/2}} \frac{\gamma_L}{\gamma_D^2} \tag{4.34}$$

$$\phi_{V_v} = \frac{1}{\pi^{3/2}} \frac{\gamma_L}{\gamma_D^2} \tag{4.35}$$

Now that the final distribution profile has been developed, it is converted to wavelength:

$$\phi_{V_\lambda} = \frac{1}{\pi^{3/2}} \frac{\gamma_L}{\gamma_D^2} \frac{c_0}{\lambda_0^2} \tag{4.36}$$

This ϕ_{V_λ} Voigt probability profile (which has units of cm^{-1}) is used to compute the absorption and emission coefficients due to radiation for particular natural frequencies.

4.3. Absorption and Emission Coefficients

As previously mentioned, there are three radiative mechanisms for a non-scattering medium; these include spontaneous emission, stimulated emission, and absorption. Through the use of this quantum mechanical theory, absorption and emission coefficients associated with each of these transitions may be developed. In order for these to be

modelled, it is necessary to utilize the tabulated quantum data for persistent lines of neutral

atoms N, O, and H. To accomplish this, the degeneracies (g), among other atomic

information, of the transitional center-line wavelengths are considered to develop the

necessary broadening profiles. The atomic degeneracies are functions of the orbital

configurations and there exists a unique pair for each upper and lower energy level. These

values were attained from a published paper of atomic data by NIST, and combined with the

corresponding quantum data. By combining Equation (4.10) and Equation (4.15), a single

effective absorption coefficient for a particular natural frequency can be developed.

$$\kappa_\nu = (n_l - n_u) g_u B_{ul} h\nu \phi_\nu \tag{4.37}$$

Similarly, a spontaneous spectral emission coefficient can be represented in terms

of the spontaneous electron decay from upper energy level U:

$$\epsilon_\nu = \frac{1}{4\pi} g_u n_u A_{ul} h\nu \phi_\nu \tag{4.38}$$

Note, B_{ul} here carries units of $\frac{cm^2}{erg\ s}$ and is with respect to frequency. However,

this definition of the Einstein coefficient is unit incompatible and incorrect to be mutually

used for wavelength. Thus, before absorption and emission coefficients can be redefined

for a new spectral variable, it is necessary to redefine the Einstein coefficient for

stimulated emission B_{ul}. Converting Equation (4.4) yields to wavelength:

$$B_{ul_\lambda} = A_{ul} \frac{\lambda^3}{8\pi hc_0} \frac{d\lambda}{d\nu} \tag{4.39}$$

where $d\lambda/d\nu$ is equivalently λ^2/c_0 (neglecting the preceding negative which flips

the limits of integration). Making this substitution produces the following definition:

$$B_{ul_\lambda} = A_{ul} \frac{\lambda^5}{8\pi h c_0^2} \tag{4.40}$$

Now, B_{ul} carries units of $\frac{cm^3}{erg}$ and is now correctly defined for use with

wavelength. Converting the rest of Equation (4.37) and Equation (4.38) yields:

$$\kappa_\lambda = (n_l - n_u)g_u B_{ul_\lambda} h \frac{c_0}{\lambda} \phi_\lambda \tag{4.41}$$

$$\epsilon_\lambda = \frac{1}{4\pi} g_u n_u A_{ul} h \frac{c_0}{\lambda} \phi_\lambda \tag{4.42}$$

In both of these above equations, the normalized Voigt profile is implemented as

the probability distribution profile ϕ_λ. In an effort to reduce the number of computations

required during each iteration of the flow field, normalized coefficients are developed by

dividing Equations (4.41) and (4.42) through by the atomic number density, n_a, yielding

(Sohn, 2011):

$$\kappa_\lambda^* = \frac{\kappa_\lambda}{n_a} = \kappa_\lambda^c \left(\frac{n_l}{n_a} - \frac{n_u}{n_a}\right) \phi_\lambda \tag{4.43}$$

$$\epsilon_\lambda^* = \frac{\epsilon_\lambda}{n_a} = \epsilon_\lambda^c \frac{n_u}{n_a} \phi_\lambda \tag{4.44}$$

Here, κ_λ^c and ϵ_λ^c are the assembled parameter coefficients and can be pre-

calculated and databased prior to running the code due to their flow field independence.

These coefficients are defined as follows;

$$\kappa_\lambda^c = g_u A_{ul} \frac{\lambda^4}{c_0} \tag{4.45}$$

$$\epsilon_\lambda^c = \frac{1}{4\pi} g_u A_{ul} h \frac{c_0}{\lambda} \tag{4.46}$$

To ensure proper development of the assembled parameter coefficients, their

values were validated for atomic Nitrogen and Oxygen using Sohn's published values. To determine the electron population density at the upper and lower energy levels (n_l/n_a and n_u/n_a), the Boltzmann's distribution is used for equilibrium flow conditions:

$$\frac{N_i}{N_a} = \frac{g_i \exp(-e_i/kT)}{\sum_i^j g_i exp\,(-e_i/kT)} \tag{4.47}$$

Where i denotes the energy and degeneracy for a particular energy level, and j is the total number of levels for the particular atomic species at a certain state.

4.4. Diffusion Approximation

Now that the emission and absorption coefficients have been defined for individual transitions, it is necessary to unify their respective values under a single weighted profile. This is accomplished through the use of the diffusion approximation, also called the Rosseland approximation, which allows for the computation of an effective radiative thermal conductivity. This allows the development of radiative thermal conductivity that can be easily implemented into a CFD code. The convenient-to-use diffusion approximation is defined as follows:

$$q_r = -\beta_R \nabla T \tag{4.48}$$

with q_r being the radiative heat flux of the model and β_R the radiative thermal conductivity. The radiative thermal conductivity (β_R) is inversely proportional to the Rosseland-mean absorption coefficient (κ_R), and is defined through the following relationship;

$$\beta_R = \frac{16n^2\sigma T^3}{3\kappa_R} \tag{4.49}$$

The radiative thermal conductivity defined above in Equation (4.49) utilizes the optically thick assumption to create a weighted profile for the electronic transitions which is incorporated by κ_R. This profile considers the individual line absorption coefficients which are weighted by the black-body intensity change with temperature (dI_{b_λ}/dT) (Modest, 2013):

$$\kappa_R = \frac{4\sigma T^3}{\pi} \frac{1}{\int_{-\infty}^{+\infty} \frac{1}{\kappa_\lambda} \frac{dI_{b\lambda}}{dT} d\lambda} \tag{4.50}$$

where σ is the Stephan-Boltzmann constant and $dI_{b\lambda}/dT$ is the change in black-body intensity with respect to temperature. The black-body intensity functions as the weighting function for an individual line transition, and is defined as the following (Modest, 2011);

$$I_{b\nu} = \frac{1}{4\pi} \frac{A_{ul}}{B_{ul}} \frac{1}{(g_l B_{lu}/g_u B_{ul}) e^{h\nu/kT} - 1} \tag{4.51}$$

Recalling the relations between the three Einstein coefficients (Equations (4.4) and (4.5)), Equation (4.51) can be reduced to the following:

$$I_{b\nu} = \frac{2h\nu^3}{c_0^2} \frac{1}{e^{h\nu/kT} - 1} \tag{4.52}$$

Here, I_{b_ν} carries units of $\frac{erg}{m^2}$. The next step is to convert this intensity to be with respect to wavelength. However, as before, B_{ul} changes with the spectral variable, and thus needs to be converted as well. The resultant black-body intensity for wavelength can be written as follows:

$$I_{b\lambda} = \frac{2hc_0^2}{\lambda^5} \frac{1}{e^{hc_0/\lambda kT} - 1} \tag{4.53}$$

The intensity I_{b_λ} now carries units of $\frac{erg}{s\,cm^3}$. Taking the derivative of Equation (4.53) with respect to temperature provides the change in black-body intensity with the respect to the fluctuations of the thermal energy of the flow field, which carries units of $\frac{erg}{s\,cm^3 K}$.

$$\frac{dI_{b\lambda}}{dT} = \frac{2h^2 c_0^3}{\lambda^6 k} \frac{e^{hc_0/\lambda kT}}{T^2 \left(e^{\frac{hc_0}{\lambda kT}} - 1\right)^2} \tag{4.54}$$

As previously mentioned, although modeling of line broadening was performed, its effects were not considered. When computing the Rosseland-mean absorption coefficient (and all preceding formulas), only the centerline wavelengths about which they are distributed are considered ($\Delta\lambda = 0$). Since discrete wavelengths are being considered, the profile distributes the centerline-weighted intensities over some finite distance $d\lambda$. Considering that each line profile has its largest contribution near the line center and decays as it extends across the wavelength spectrum, the entire line need not be accounted for. For this reason, each line was distributed across a $d\lambda$ which was approximated to be equal to the Doppler line half-width. This was done due to the spectral dependence of the line half-width. Once the radiative thermal conductivity is determined, it was implemented into a CFD code and analyzed against a purely convection-contributed hypersonic case.

5. Approach

The diffusion approximation is derived based on the *optically thick* assumption. Therefore, for this study, the flow is considered to be purely optically thick, and thus the radiation can be called "Black-body". Black-body radiation is an ideal radiation absorber and has properties of being a non-reflective medium that is in thermodynamic equilibrium with its environment. This type of radiation depends only on the temperature of the surrounding body and is defined by a continuous spectrum. In an effort to reduce the computational time required for the CFD code, assembled parameter coefficients that were independent of flow field conditions were developed. The computation simulated a simple radiation example limited to first order in space.

Once the net total absorption and emission coefficients were developed for individual transitions of the three atoms in consideration, their individual effects were weighted and implemented using Wilke's mixing rule. Since the diffusion approximation allows for the convenient development of an effective radiative thermal conductivity, this is added to the general thermal conductivity of the flow field medium. However, since the relative contribution of the radiative thermal conductivity at lower temperatures is insignificant, it is only implemented into the flow field where the temperature is greater than 6000 K.

In an effort to better visualize the effects of radiative heat transfer on hypersonic reentry flow, the flow over a geometrically simple 2-D blunt body is considered. The blunt body geometry used was a cylinder which was 1 cm in diameter. For simplicity, only one half of the cylinder was modelled and symmetry conditions were implemented. The free stream velocity was 8000 m/s ($M \cong 17$) with a pressure of 0.1 atmospheres and

temperature of 217°K. This speed was chosen to induce temperature fields that were high

enough to significantly show the effects of implementing an effective radiative

conductivity. The flow field considers a dissociated atmosphere consisting of 79% atomic

Nitrogen and 21% atomic Oxygen. Additionally, the viscosity and wall slip were

implemented for the CFD computations of the blunt body. The surface boundary

condition for this blunt body CFD model was laminar viscous, adiabatic, no slip wall.

The CFD code used in this study was a structured, 3D unsteady, viscous, and

compressible Navier-Stokes solver used for modeling fluid thermophysics on hypersonic

aerospace vehicles and propulsion applications. The numerical scheme used is the

modified Steger-Warming Flux Vector Splitting, an upwind differencing scheme used for

its capabilities of modeling shock waves. This method decomposes the inviscid flux into

two separate parts, positive and negative, in relation to the sign of the eigenvalues.

6. Results of Calculations

6.1. Transition-Specific Absorption Coefficients

It is necessary to model the absorption and emission coefficients produced by the individual electronic transitions before they can be implemented into a more general model. Using available data for electronic energy levels, Einstein coefficients, and degeneracies, the assembled parameter coefficients for absorption and emission, κ_λ^c and ϵ_λ^c respectively were developed and stored. These flow-field independent values for Nitrogen and Oxygen were verified for order conformity to the results published by Sohn. Yet, a line-to-line comparison of the data was unable to be performed. This was due to Sohn using the NEQAIR database for acquiring molecular data whereas this research utilized the NIST database, which contains few overlapping data points. However, the computed assembled-parameter coefficients were shown to be in agreement as seen below for Nitrogen (Table 6.1 for Sohn and Table 6.2 for calculated) and Oxygen (Table 6.3 for Sohn and Table 6.4 for calculated). Once these parameters are calculated, they are stored and called as a single variable in the flow field dependent calculations.

Table 6.1 Data sets for ϵ_λ^c and κ_λ^c for atomic Nitrogen from Sohn (Sohn, 2011)

Wavelength(Å)	ϵ_λ^c (W/sr)	κ_λ^c (cm³)	Upper (NEQAIR	Lower Indices)
1101.276	2.841×10^{-11}	3.8633×10^{-24}	12	2
1134.725	6.962×10^{-11}	1.0966×10^{-23}	5	1
1134.975	1.392×10^{-10}	2.2012×10^{-23}	5	1
1135.535	1.837×10^{-10}	2.9113×10^{-23}	5	1
1164.412	2.605×10^{-13}	4.6820×10^{-25}	10	2

Table 6.2 Calculated data sets for ϵ_λ^c and κ_λ^c for atomic Nitrogen

Wavelength (Å)	ϵ_λ^c (W/sr)	κ_λ^c (cm³)
1199.55	3.22E-10	3.606E-23
1200.22	2.12E-10	2.158E-23
1200.71	1.05E-10	7.217E-24

Table 6.3 Data sets for ϵ_λ^c and κ_λ^c for atomic Oxygen from Sohn (Sohn, 2011)

Wavelength(Å)	ϵ_λ^c (W/sr)	κ_λ^c (cm³)	Upper (NEQAIR	Lower Indices)
807.365	1.374×10^{-10}	3.957×10^{-24}	19	1
879.450	7.007×10^{-11}	3.095×10^{-24}	19	1
879.538	2.156×10^{-10}	9.526×10^{-24}	19	1
880.599	5.742×10^{-11}	2.553×10^{-24}	19	1
880.648	4.252×10^{-11}	1.891×10^{-24}	19	1

Table 6.4 Calculated data sets for ϵ_λ^c and κ_λ^c for atomic Oxygen

Wavelength (Å)	ϵ_λ^c (W/sr)	κ_λ^c (cm³)
1302.17	1.15E-10	6.710E-23
1304.86	6.80E-11	4.429E-23
1306.03	2.26E-11	2.207E-23

Once the assembled parameter values were verified, the next step of validation was to verify the accuracy of the coefficients of emission (ϵ_λ) and absorption (κ_λ) which are dependent on the flow field conditions (these being temperature, pressure, and molecular composition). As previously mentioned, for simplicity, the broadening effects from the centerline frequencies for each of the atomic structures were not considered. Instead, a discrete summation of the natural frequencies of the neutral atoms was performed. In doing this, it was observed that the emission coefficients were generally over-predicted from peak frequencies. However, the averaged absorption coefficient was generally under-predicted from the peak values.

In an effort to visualize comparison between the averaged coefficients and the coefficients which considered full line broadening (Sohn, 2011), plots are utilized for benchmarking of how each of the values rank. Since Sohn only considers atomic Nitrogen and Oxygen for emission and absorption, these are the only two which elements for which a comparison could be made. It should be noted that as well as consideration of line broadening, Sohn also utilizes Stark broadening as well as a less-conventional definition for the Voigt profile. This method was not followed since much of the atomic and molecular data and coefficients utilized by Sohn derived directly from NEQAIR calculated values and are not publicly available without licensure.

Table 6.5, shown below, lists the absorption and emission coefficients for single line transitions of atomic Nitrogen, Oxygen, and Hydrogen. These values can be compared to Figure 6.1 for Nitrogen and Figure 6.2 for Oxygen which displays the wavelength-specific characteristics of the absorption and emission coefficients. The peaks observed represent the locations of natural frequencies as shown from line

broadening methods. The full table of these values for each of the molecular species can

be seen in the Appendix.

Table 6.5 Sample calculated absorption and emission coefficients at P = 0.1 atm, T = 17485 K, $n_a = 1.1513 \; x \; 10^{15} \; cm^{-3}$ for validation to Sohn

Atomic Species	κ_λ (cm^{-1})	ϵ_λ (erg/s-cm³-sr-μm)	γ_L (s⁻¹)	γ_D (s⁻¹)
Nitrogen	2.591E-03	4.009E+07	3.34E+06	3.16E+10
Oxygen	2.896E-03	2.058E+07	2.96E+06	2.73E+10
Hydrogen	2.673E-05	4.387E+07	4.95E+05	2.37E+10

When analyzing the below plots, the calculated spontaneous emission coefficient

(ϵ_λ) is near the peak values of the distributed emission coefficient from Sohn. Because a

discrete summation is being performed of the natural frequencies, it is expected that these

coefficients are the peak orders of magnitude. However, it is observed that for the

effective absorption coefficient (κ_λ), the computed value is near the mid-peak. This is

likely due to the differences in line data available that coincide with Sohn's. Additionally,

this research extends into a higher range of natural frequencies than Sohn, where the

orders of magnitude for the line peaks are much smaller. Considering that Sohn's

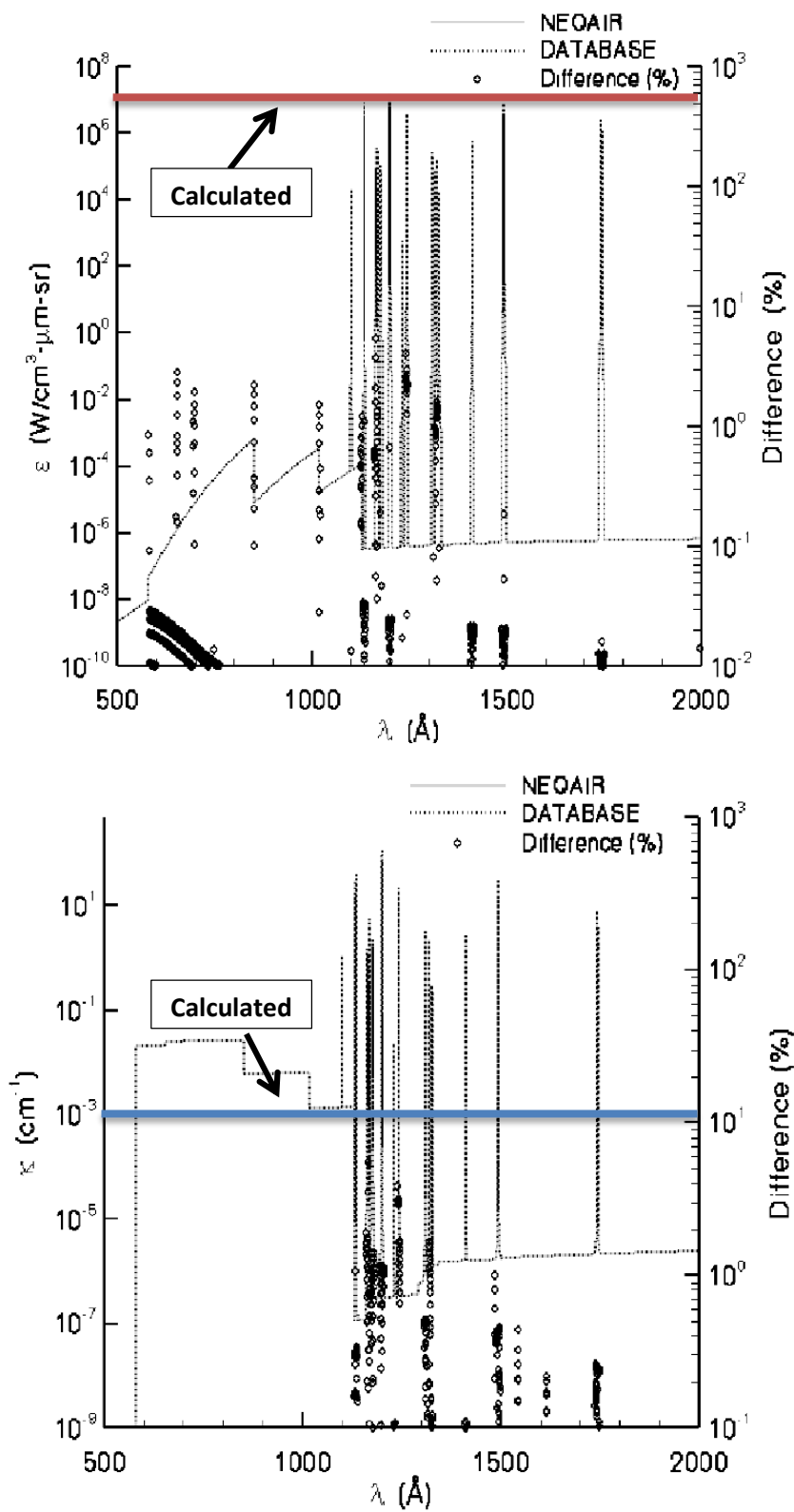research was focusing on the lower natural frequency band, this result is expected.

Figure 6.1 Emission (Top) and absorption (Bottom) coefficients determined by Sohn for atomic Nitrogen (Sohn, 2011)
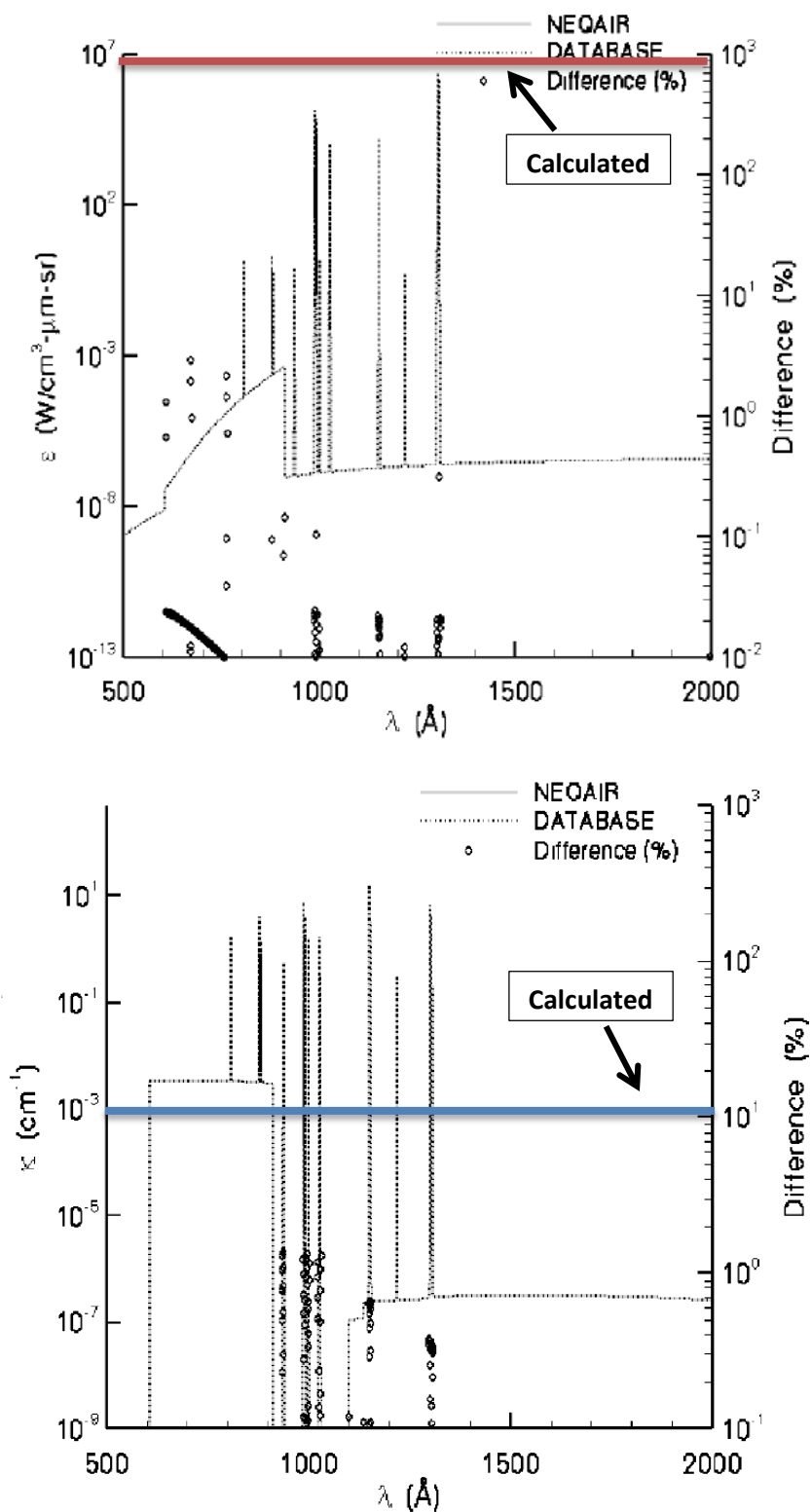
Figure 6.2 Emission (Top) and absorption (Bottom) coefficients determined by Sohn for atomic Oxygen (Sohn, 2011)

6.2. Diffusion Approximation Implementation and Demonstration

The radiative thermal conductivities were computed versus temperature at a constant pressure of 0.1 atm (Figure 6.3). Additionally, it should be noted that while the Rosseland (diffusion) approximation works well for the center of the media, its breaks down near physical boundaries. This is because at these boundaries, it is unable to account for the "long range" radiation effects (Irvine & Hartnett, 1966). This means, near boundaries, the length distance for intensity change can become on the order of the photon mean free path. Therefore, outside of very large optically thick dimensions in the media, the radiative heat flux will be calculated with considerable error. It has been shown that near physical boundaries, there exists a discontinuity in the form of a temperature spike between the wall and the medium it is adjacent to.
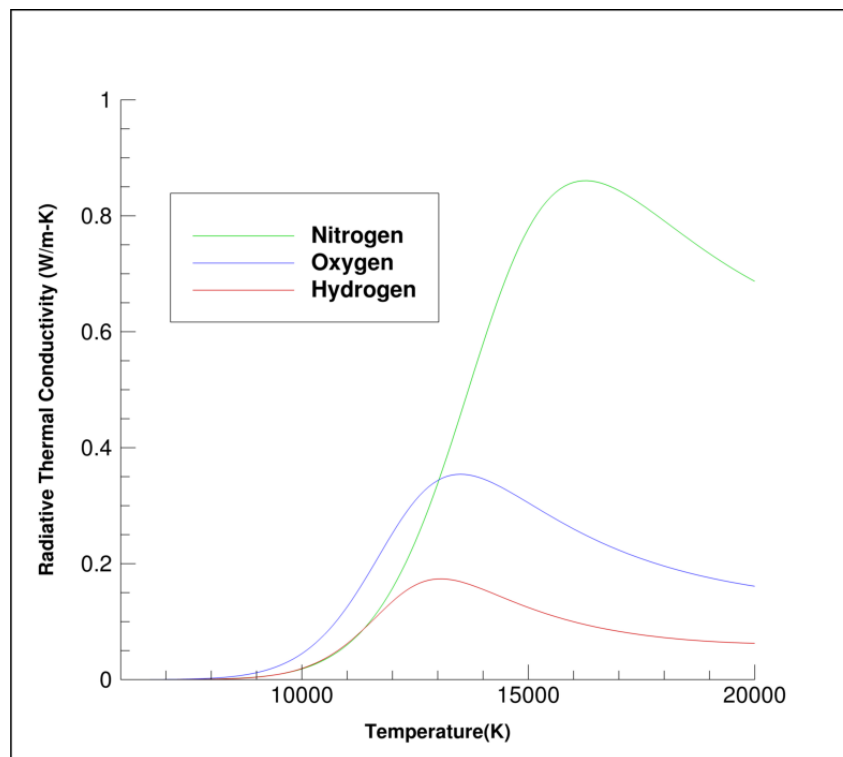

Figure 6.3 Functionality of radiative conductivity

It was desired to observe the differences (if any) in the temperature fields for the blunt body geometry in hypersonic flow. Two identical flow fields were constructed and computed with one considering purely convective modeling and the other considering radiation (via the diffusion approximation). It was anticipated that due to the higher total thermal conductivity when considering radiation, the flow field would be more diffuse with a lower total temperature. This is particularly true since this diffusion approximation does not consider spontaneous emission effects, i.e. there are no *sources* of energy. Additionally, because the radiation models only are included at temperatures above 6000°K, this value was used as the lower limit for observing temperature field changes. The CFD temperature field for this comparison is shown in Figure 6.4 for the non-radiative flow field and Figure 6.5 for radiation.
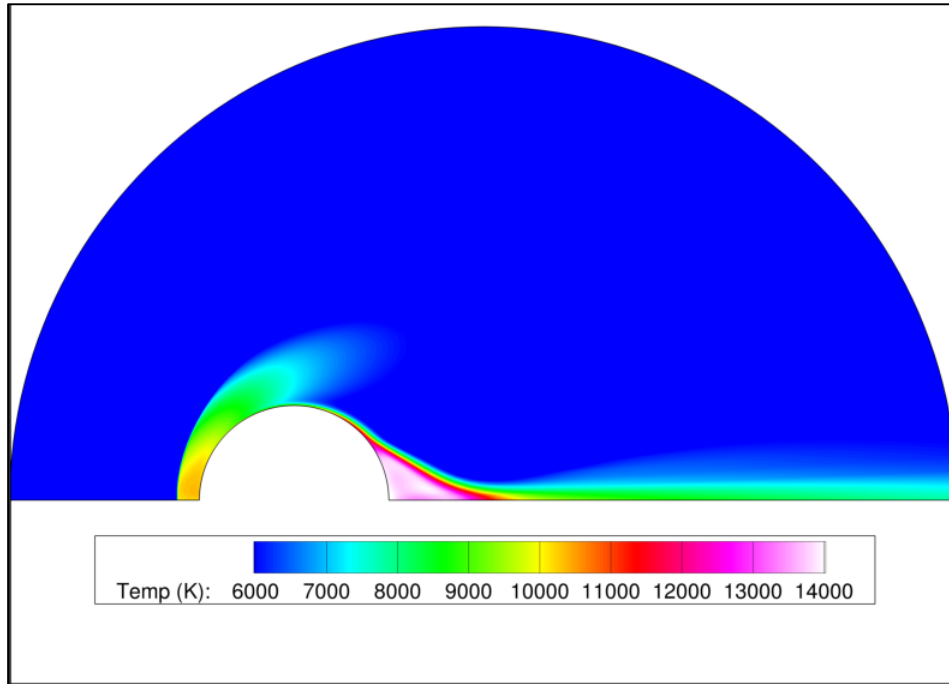
Figure 6.4 Temperature field without radiation modeling
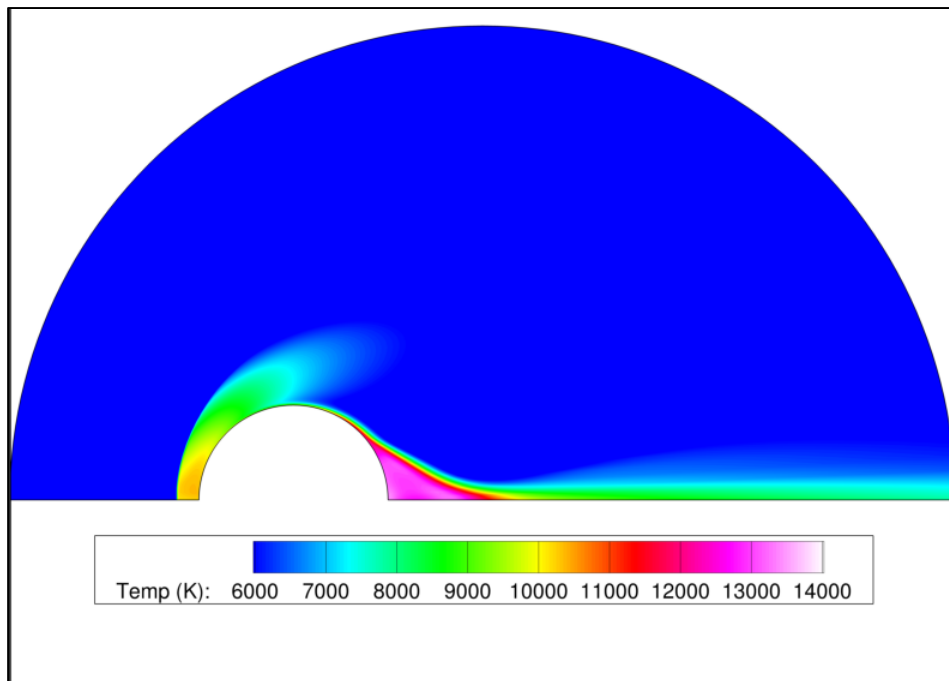
Figure 6.5 Temperature field with radiation modeling

In the flow field which does not consider radiative effects, the peak temperature observed is approximately 14,000°K, in the shear layer behind the blunt body. In the calculation considering radiation, a peak temperature of approximately 13,300°K was observed. In both of these cases, a high temperature region was observed behind the blunt body in the recirculation region below the point of flow separation.
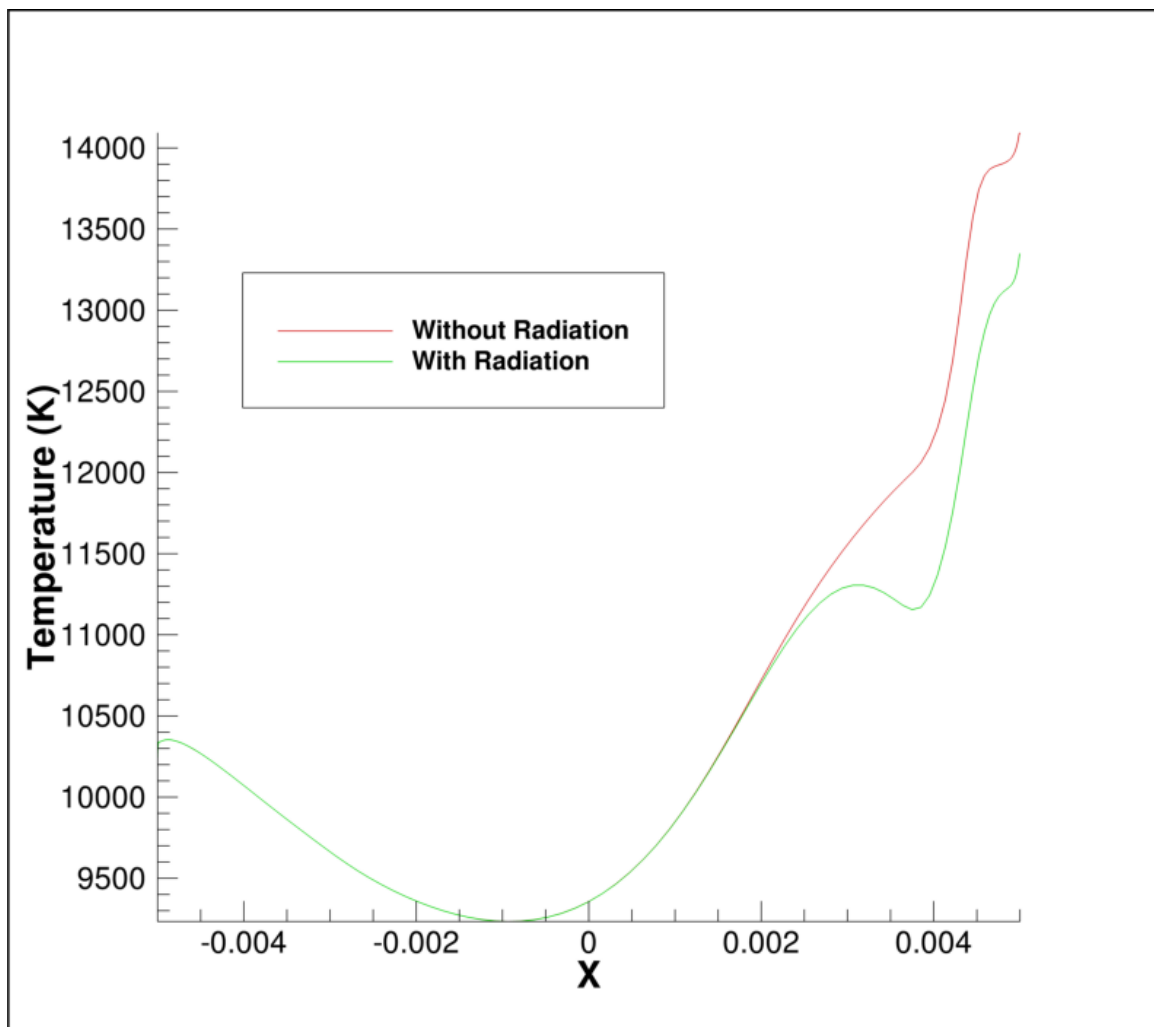
Figure 6.6 Temperature over the blunt body surface

Figure 6.6 shows the surface temperature from the leading to trailing edge for both the radiative and non-radiative cases. It is observed that temperature is nearly identical across the front face of the blunt body, but as temperatures increase on the back of the geometry, the two lines diverge. This divergence is due to the increased diffusivity of the temperature field when implementing the radiative conductivity and thus results in a peak temperature that is approximately 700°K cooler than the purely convective case.

An investigation was performed to understand why the highest temperatures existed behind the blunt body opposed to the front (facing the bow shock). As seen below in Figure 6.7, the regions of low kinetic energy were isolated in the Mach 17 flow and shown to exist in two zones; a stagnation region of trapped air at the front and a recirculation region in the back. However, the trailing region contains a region of very high kinetic energy. This arises due to the low order of the model. Since this model is computed at first order in space, this media in the recirculation region is effectively "trapped" behind the blunt body instead of shedding away. However, this provides for a high temperature region to exist which illustrates the diffusive effects incurred in the flow field when radiation models are considered.
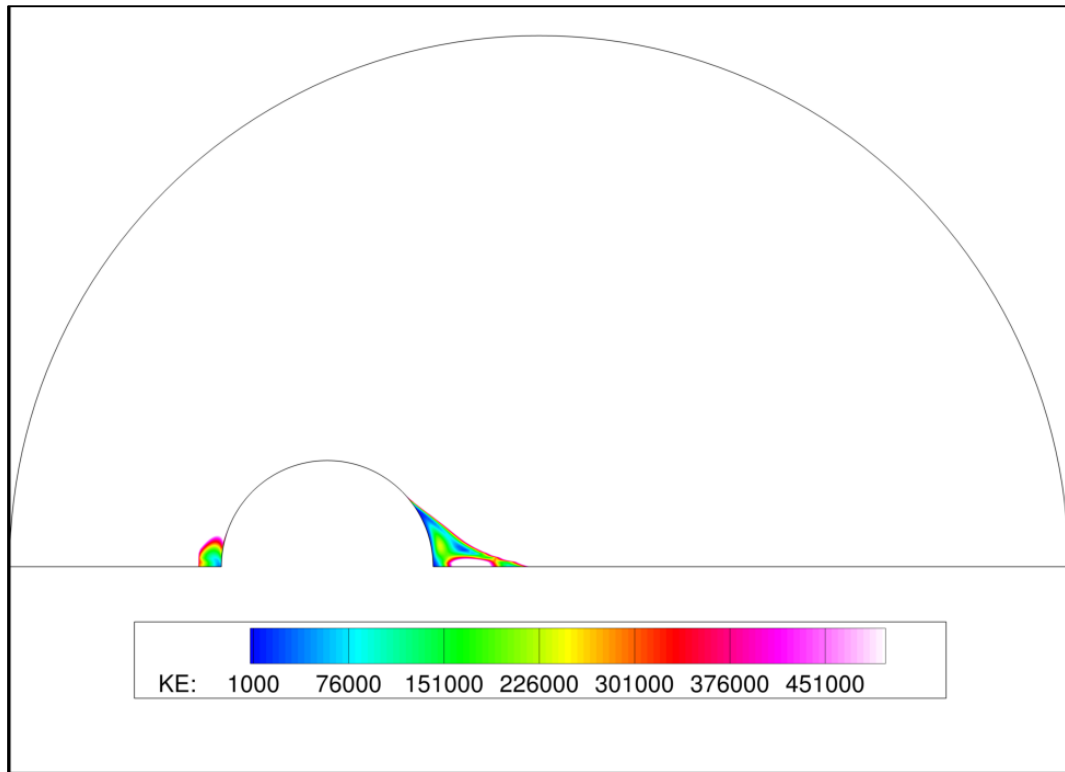
Figure 6.7 Kinetic energy of the blunt body flow field

7. Conclusion

This research found that there is a notable difference between a purely convective flow field and one which considers radiation when considering high Mach number flow. The flow field-independent parameterized absorption and emission coefficients which were databased showed good agreement with Sohn's published findings. Additionally, when utilizing the same initial conditions as Sohn in the discretely-summed model, similar absorption and emission coefficients were observed for both atomic Nitrogen and Oxygen.

At high temperatures and Mach numbers, the contribution of radiative heat transfer was seen to become largely significant and even dominant over purely-convective heat transfer. It was observed that the thermal conductivity for radiation becomes comparable to the purely-convective conductivity around 10,000°K, and dominant at temperatures above 11,000°K. The effect of this increase in thermal conductivity is a more diffuse temperature field in regions of high thermal energy. Thus, it is essential to account for radiation when performing high Mach number hypersonic flow analysis to provide a more true representation of the temperature field around a blunt body.

This research aided in improving HYP's heat transfer analysis in hypersonic reentry flows. The analysis and understanding of heat transfer and ultimately mitigation is an essential aspect of space travel and exploration.

8. Future Work

There is still more work to be done on the implementation of more complete line broadening models to develop a more accurate representation of the individual line absorption and emission coefficients. Also, the current configuration of this model only considers neutral atomic nitrogen, oxygen, and hydrogen. It is desired to implement the molecular combinations of these elements as well as singly ionized versions of these elements so that a more accurate representation of the atmospheric conditions can be created for analysis. Finally, future work may also include modeling transitions due to rotational and vibrational transitions for diatomic molecules.

REFERENCES

Anderson, J. (2006). Hypersonic and high-temperature gas dynamics (2nd ed.). Reston, Va.: American Institute of Aeronautics and Astronautics.

Nutzati, J. (2013). Computing Radiation Exchange, Master's Thesis, Embry-Riddle Aeronautical University.

Perrell, E., Power, G., & Robinson, C. (2010). A Modular Conjugate Heat Transfer Capability for the Wind-US CFD Code, AIAA 2010-31, 48th AIAA Aerospace Sciences Meeting, Orlando, FL.

Nutzati, J. & Perrell, E. (2013). Modeling Radiative Heat Exchange for a Supersonic Flow, AIAA 2013-0449, 51st Aerospace Sciences Meeting, Grapevine, TX.

Engblom, W., Fletcher, B., & Georgiadis N. (2007). Validation of Conjugate Heat Transfer Capability for Water-Cooled High-Speed Flows, AIAA 2007-4392, 39th AIAA Thermophysics Conference, Miami.

Fletcher, B. (2007). Validation of Conjugate Heat Transfer Capability for Water-Cooled High-Speed Flows, Master's Thesis, Embry-Riddle Aeronautical University.

Brandis, A., Laux, C., Magin, T., Mcintyre, T., & Morgan, R. (2014). Comparison of Titan Entry Radiation Shock-Tube Data with Collisional-Radiative Models. Journal of Thermophysics and Heat Transfer, 1-7.

Goldsworthy, M. (2012). Modeling of electronic excitation and radiation in the Direct Simulation Monte Carlo Macroscopic Chemistry Method. Physics of Fluids, 106102-106102.

Rosseland, S. (1936). Theoretical Astrophysics, Atomic Theory, and the Analysis of Stellar Atmospheres and Envelopes," Clarendon Press, Oxford.

Li, Z., Ozawa, T., Sohn, I., & Levin, D. (2011). Modeling of electronic excitation and radiation in non-continuum hypersonic reentry flows. Physics of Fluids, 066102-066102.

Mazaheri, A., Johnston, C., & Sefidbakht, S. (2013). Three-Dimensional Radiation Ray-Tracing for Shock-Layer Radiative Heating Simulations. Journal of Spacecraft and Rockets, 485-493.

Allen, J., & Eggers, A., Jr. (1953). A Study of the Motion and Aerodynamic Heating of Ballistic Missiles Entering the Earth's Atmosphere at High Supersonic Speeds.

Whiting, E. E., Park, C., Liu, Y., Arnold, J. O., & Paterson, J. A. (1996). NEQAIR 96 User Manual, Tech. rep., NASA Ames Research Center, Moffett Field, CA.

Mazaheri, A. (2010). LAURA users manual, 5.3-48528. Hampton, Va.: National Aeronautics and Space Administration, Langley Research Center.

Pierrot, L., Laux, C., & Kruger, C. (1998). Vibrationally-specific collisional-radiative model for nonequilibrium nitrogen plasmas. 29th AIAA, Plasmadynamics and Lasers Conference.

Johnston, C. (2006). Nonequilibrium Shock-Layer Radiative Heating for Earth and Titan Entry, Ph.D. thesis, Virginia Polytechnic Institute and State University.

Modest, M. F. (2013). Radiative Heat Transfer, 3rd ed., American Press, Oxford, Chaps. 10, 11, 15.

Anderson, J. D. Jr. (1995). Computational Fluid Dynamics: The basics with applications, 1st ed., McGraw-Hill, New York, Chap. 11

Sohn, I. (2011). Modeling and Simulation from hypersonic flows with Monte Carlo methods.

Huang, X., & Yung, Y. (2003). A Common Misunderstanding about the Voigt Line Profile. Journal of the Atmospheric Sciences, 1630-1632.

Wiese, W., Smith, M., & Glennon, B. (1966). Atomic Transition Probabilities. National Standard Reference Data Series, 1.

Sansonetti, J., & Martin, W. (n.d.). Handbook of Basic Atomic Spectroscopic Data. Retrieved March 8, 2015, from http://www.nist.gov/pml/data/handbook/index.cfm

Slater, J. (1964). Atomic Radii in Crystals. The Journal of Chemical Physics, 3199-3199.

Goody, R., & Yung, Y. (1995). Atmospheric radiation theoretical basis (2nd ed.). New York: Oxford University Press.

Penner, S. (1959). Quantitative molecular spectroscopy and gas emissivities. Reading, Mass.: Addison-Wesley Pub.

Park, C. (1990). Nonequilibrium hypersonic aerothermodynamics. New York: Wiley.

Irvine, T., & Hartnett, J. (1966). Advances in Heat Transfer, 3. Burlington: Elsevier.

APPENDIX

Flow-Independent Atomic Parameters

Flow-Independent Atomic Parameters for Nitrogen (N)

Wavelength (Å)	ϵ_λ^c (erg/s-sr)	κ_λ^c (cm³)	A_{UL} ($10^8\ s^{-1}$)	Lower energy level L (e_L), (cm)	Upper energy level U (e_U), (cm)	Degeneracy at level L (gl)	Degeneracy at level U (gU)
1199.55	3.22E-03	3.606E-23	4.07	0	83364.62	4	6
1200.22	2.12E-03	2.158E-23	4.02	0	83317.83	4	4
1200.71	1.05E-03	7.217E-24	4	0	83284.07	4	2
1243.18	2.45E-03	1.251E-20	3.21	19224.464	99663.427	6	6
1492.63	1.33E-03	8.944E-21	3.13	19224.464	86220.51	6	4
1742.73	4.21E-04	5.370E-21	1.16	28839.306	86220.51	4	4
7442.29	1.05E-05	1.957E-20	0.124	83317.83	96740.84	4	4
7468.31	1.63E-05	1.958E-20	0.193	83364.62	96740.84	6	4
8680.28	3.58E-05	1.958E-20	0.246	83364.62	94881.82	6	8
8683.40	1.97E-05	3.918E-20	0.18	83317.83	94830.89	4	6
12469.62	2.31E-05	1.423E-20	0.228	96864.05	104881.35	6	8

Flow-Independent Atomic Parameters for Oxygen (O)

Wavelength (Å)	ϵ_λ^c (erg/s-sr)	κ_λ^c (cm³)	A_{UL} ($10^8\ s^{-1}$)	Lower energy level L (e_L), (cm)	Upper energy level U (e_U), (cm)	Degeneracy at level L (g_L)	Degeneracy at level U (g_U)
1302.17	1.15E-03	6.710E-23	3.15	0	76794.978	5	3
1304.86	6.80E-04	4.429E-23	1.87	158.265	76794.978	3	3
1306.03	2.26E-04	2.207E-23	0.623	226.977	76794.978	1	3
7771.94	5.25E-05	6.105E-23	0.369	73768.2	86631.454	5	7
7774.17	3.75E-05	8.248E-23	0.369	73768.2	86627.778	5	5
7775.39	2.25E-05	5.680E-23	0.369	73768.2	86625.757	5	3
8446.25	5.42E-05	2.019E-21	0.322	76794.978	88631.303	3	9
8446.36	5.42E-05	3.187E-21	0.322	76794.978	88631.146	3	9
8446.76	5.42E-05	1.483E-20	0.322	76794.978	88630.587	3	9
9266.01	6.83E-05	8.149E-21	0.445	86631.454	97420.63	7	9
13164.85	4.29E-06	5.853E-20	0.119	88631.146	96225.049	9	3

Flow-Independent Atomic Parameters for Hydrogen (H)

Wavelength (Å)	ϵ_λ^c (erg/s-sr)	κ_λ^c (cm³)	A_{UL} $(10^8 s^{-1})$	Lower energy level L (e_L), (cm)	Upper energy level U (e_U), (cm)	Degeneracy at level L (g_L)	Degeneracy at level U (g_U)
949.74	3.43E-04	2.227E-24	0.34375	0	105291.64	2	6
972.54	6.65E-04	4.858E-24	0.6819	0	102823.88	2	6
1025.72	1.55E-03	1.474E-23	1.6725	0	97492.284	2	6
1215.67	4.89E-03	1.090E-22	6.2648	0	82259.285	2	6
1215.67	4.89E-03	1.090E-22	6.2649	0	82258.919	2	6
4340.46	1.84E-06	2.384E-23	0.0253	82259.111	105291.66	6	2
4340.46	5.53E-06	7.151E-23	0.0253	82259.111	105291.66	2	6
4340.46	9.21E-06	1.192E-22	0.0253	82259.111	105291.66	6	10
4861.28	5.59E-05	1.274E-21	0.1719	82258.919	102823.89	6	10
4861.29	1.89E-05	4.300E-22	0.0967	82258.954	102823.89	2	6
4861.36	6.71E-05	1.529E-21	0.2063	82259.285	102823.91	6	10
6562.71	1.30E-04	1.326E-20	0.5388	82258.919	97492.32	6	10
6562.72	3.24E-05	3.316E-21	0.2245	82258.954	97492.32	2	6
6562.85	1.56E-04	1.592E-20	0.6465	82259.285	97492.356	6	10
12818.07	1.63E-06	4.729E-21	0.022	97492.309	105291.66	2	6
12818.07	5.43E-07	1.576E-21	0.022	97492.309	105291.66	6	2
12818.07	2.71E-06	7.882E-21	0.022	97492.309	105291.66	6	10
12818.07	1.63E-06	4.729E-21	0.022	97492.309	105291.66	10	6
12818.07	3.80E-06	1.103E-20	0.022	97492.309	105291.66	10	14
18751.01	4.55E-06	8.850E-20	0.0899	97492.309	102823.9	2	6
18751.01	1.52E-06	2.950E-20	0.0899	97492.309	102823.9	6	2
18751.01	7.58E-06	1.475E-19	0.0899	97492.309	102823.9	6	10
18751.01	4.55E-06	8.850E-20	0.0899	97492.309	102823.9	10	6
18751.01	1.06E-05	2.065E-19	0.0899	97492.309	102823.9	10	14